Journal of
Applied Physics

RESEARCH ARTICLE | FEBRUARY 26 2026

# Thermal and mechanical behavior of plasma-synthesized, nanometer scale aluminum fluoride passivation layers

Mohsen Motezaker ; Andrew H. Jones ; David R. Boris ; Scott G. Walton ; Patrick E. Hopkins ✉

*J. Appl. Phys.* 139, 085109 (2026)
https://doi.org/10.1063/5.0313146

AIP Publishing

Journal of
Applied Physics
ARTICLE
pubs.aip.org/aip/jap

# Thermal and mechanical behavior of plasma-synthesized, nanometer scale aluminum fluoride passivation layers

Cite as: J. Appl. Phys. **139**, 085109 (2026); doi: 10.1063/5.0313146
Submitted: 20 November 2025 · Accepted: 4 February 2026 ·
Published Online: 26 February 2026

Mohsen Motezaker,[1] Andrew H. Jones,[2] David R. Boris,[3] Scott G. Walton,[3]
and Patrick E. Hopkins[1,2,4,5,a)]

AFFILIATIONS

[1] Department of Mechanical and Aerospace Engineering, University of Virginia, Charlottesville, Virginia 22904, USA
[2] Laser Thermal, Charlottesville, Virginia 22902, USA
[3] U.S. Naval Research Laboratory, Plasma Physics Division, Washington, DC 20375, USA
[4] Department of Materials Science and Engineering, University of Virginia, Charlottesville, Virginia 22904, USA
[5] Department of Physics, University of Virginia, Charlottesville, Virginia 22904, USA

[a)] **Author to whom correspondence should be addressed:** peh4v@virginia.edu

## ABSTRACT

Aluminum is highly valued in ultraviolet (UV) optics for its exceptional reflectivity at wavelengths as short as 90 nm, but its effectiveness is compromised by rapid formation of a native oxide layer that reduces its UV reflectivity. To mitigate this issue, fluorine-containing protective layers, such as aluminum fluoride, are applied to inhibit oxidation while maintaining high transmission rates. Additionally, an aluminum fluoride layer serves as an effective barrier coating in advanced lithium-ion battery designs, preventing failures like significant temperature increases and thermal runaway. Despite these important applications, the thermal and mechanical properties of aluminum fluoride thin films have not been thoroughly investigated. In this study, optical pump–probe techniques are used to measure the thermal conductivity and elastic moduli of aluminum fluoride passivation layers with thicknesses ranging from 4 to 48 nm. The passivation layers are produced using a plasma-based process that removes the native oxide while converting the aluminum into aluminum fluoride. The results show that both thermal conductivity and elastic moduli increase with film thickness, indicating a thickness-dependent change in physico-chemical composition. Energy-dispersive x-ray spectroscopy reveals that thicker layers contain a higher proportion of fluorine relative to aluminum. Moreover, x-ray photoelectron spectroscopy and infrared variable-angle spectroscopic ellipsometry indicate that the chemical structure stabilizes in thicker samples, confirming the formation of $AlF_3$. These findings provide valuable insights into the process–structure–property relationships of plasma-produced fluorinated layers, which are critical for optimizing UV optical coatings and enhancing lithium-ion battery safety.

## I. INTRODUCTION

In the far ultraviolet (FUV) range (100–200 nm), aluminum is a widely utilized optical coating due to its excellent reflectivity.[1,2] This spectral range is critical for capturing key spectral lines of atomic and ionic species, such as hydrogen, carbon, nitrogen, and oxygen, which are essential in astronomy, astrophysics, solar physics, and atmospheric research.[3] However, aluminum rapidly forms a native oxide layer upon exposure to air, significantly reducing its reflectivity in the FUV range.[4] This oxidation challenge is particularly problematic for developing durable, high-reflectance FUV mirrors used in space applications, where long-term stability is essential due to the high cost and difficulty of component replacement.[5]

To address this issue, fluorine-containing protective coatings, such as magnesium fluoride ($MgF_2$) and aluminum fluoride ($AlF_3$), are commonly applied to prevent oxidation and preserve reflectivity.[6,7] $AlF_3$, in particular, is attractive due to its low index of refraction and a FUV cutoff wavelength of around 105 nm, making it highly suitable for UV optics, dielectric cavities, and as a spacer in Bragg reflective dielectric multilayers.[8,9] Furthermore, $AlF_3$ functions as a transparent, protective layer for FUV mirrors.[10] The deposition of $AlF_3$ thin films has been achieved through various methods, including physical vapor deposition, chemical vapor deposition, atomic layer deposition, and plasma-enhanced deposition techniques, each offering advantages in film quality and processing temperature.[1,11]

While the optical properties of $AlF_3$ as a protective coating are well established, its thermal and mechanical properties remain underexplored, particularly with respect to their impact on device performance in high-power optical applications.[12,13] Thermal conductivity is a critical parameter for heat dissipation in optical components subjected to high photon fluxes.[14] Insufficient thermal conductivity can lead to localized heating, thermal gradients, and subsequent thermomechanical stresses, potentially causing failure in devices such as high-power lasers and photodetectors.[15–18] Mechanical properties, such as the elastic modulus, are also crucial for the durability and reliability of thin-film coatings.[19] Mechanical stresses can arise from thermal expansion mismatch, mechanical vibrations, and external forces, leading to failures such as cracking, delamination, and wear.[20] Understanding the mechanical properties of $AlF_3$ thin films is, therefore, essential to ensure their long-term stability and performance. Beyond optics, $AlF_3$ layers are also critical as barrier coatings in advanced lithium-ion batteries. In this application, they address two primary challenges: mechanical degradation and thermal safety. Mechanical degradation, such as the cracking and pulverization of electrode particles, arises from the stresses of repeated volume changes during battery cycling.[21,22] An effective coating must have a high elastic modulus to provide structural support and prevent these failures. Simultaneously, thermal runaway, a major safety issue, can be triggered by exothermic reactions between the highly charged electrode and the electrolyte. $AlF_3$ coatings mitigate this risk primarily by acting as a chemically inert passivation layer that physically separates the electrode from the electrolyte, thereby suppressing the initial exothermic side reactions that trigger thermal runaway. Additionally, the coating aids in heat dissipation to prevent localized hot spots.[23] Therefore, the elastic modulus and thermal conductivity of the $AlF_3$ layer are the key physical properties that determine its effectiveness. Despite their importance, these properties are not well-characterized for $AlF_3$ thin films. A comprehensive understanding of both the thermal conductivity and mechanical properties is, therefore, essential for optimizing their performance and durability in these applications.

In response, this work focuses on characterizing the thermal conductivity and elastic modulus of $AlF_3$ thin films produced by plasma treatment of aluminum. The unique plasma-based process has been shown to effectively convert aluminum into $AlF_3$ while simultaneously removing the native oxide layer to develop a thin $AlF_3$ passivation layer.[24,25] Compared to oxidized aluminum, the passivated mirrors showed a dramatic (>4×) increase in FUV reflectivity down to ≈105 nm. This includes a reflectivity that exceeded 90% at the key reference FUV wavelength of the hydrogen Lyman α (121.6 nm).[24] In this work, we aim to provide insights into the process–structure–property relationships of aluminum fluoride passivation layers that will enhance the understanding of $AlF_3$'s role as a protective layer in optical systems and other advanced applications.

In this study, we employ time-domain thermoreflectance (TDTR) and steady-state thermoreflectance (SSTR) to measure the thermal conductivity of $AlF_3$ thin films,[26,27] which allows us to assess heat conduction through the films. Additionally, we used picosecond acoustics[28,29] to characterize the mechanical properties of the $AlF_3$ films by measuring the elastic modulus derived from the sound speed in the material.

## II. METHODS: SAMPLE FABRICATION, CHEMICAL ANALYSIS, THERMAL CONDUCTIVITY, AND ELASTIC MODULUS

Aluminum thin films with a thickness of ≈70 nm were deposited onto sapphire substrates by electron-beam evaporation at a base pressure of $1 \times 10^{-7}$ Torr. Prior to deposition, the sapphire substrates were first ultrasonically cleaned using isopropanol, acetone, and ethanol, then dried with air, and finally treated with $O_2$ plasma to remove organic contaminants and enhance film adhesion. To ensure sample-to-sample consistency, all the samples were created in a single deposition. After deposition, the Al films were subjected to plasma treatments using the U.S. Naval Research Laboratory's (NRL) Large Area Plasma Processing System (LAPPS)[30,31] to grow $AlF_3$ layers on the surface of the Al films. Figure 1(a) shows a schematic of the LAPPS configuration.

LAPPS employs an electron beam generated plasma[32] produced in a mixture of Ar and $SF_6$. Both Ar and $SF_6$ are introduced at flow rates of 25 SCCM to produce a total pressure of ≈30 mTorr. The system makes use of a linear hollow-cathode electron source to generate sheet-like electron beams with typical current densities of 1–5 $mA/cm^2$, and beam energies between 1 and 5 keV to drive plasma production. The system consists of the linear hollow cathode (length = 16.2 cm), an entrance aperture through which the electron beam is injected, a termination anode, and magnetic field coils. Materials are introduced at a processing stage that is oriented parallel to the direction of beam propagation and below the beam volume. In this work, the standoff distance between the beam axis and substrate is 2.5 cm. A coaxial magnetic field of 150 gauss is used to collimate the e-beam, and thus, ensure uniformity along its length.[33] The chosen magnetic field strength leaves the plasma ions un-magnetized while aiding in electron confinement. These parameters are sufficient to produce uniform plasma sheets compatible with a processing stage that accepts 150 mm diameter substrates. The processing stage can either be left at ground (unbiased) resulting in substrate bombardment by very-low-energy ions (<5 eV) or biased using either conventional DC or RF voltage to raise the ion energy.

Importantly, in highly electronegative gases such as $SF_6$ used in this work, electron beam generated plasmas enable the production of plasmas, where the dominant negative charge carriers are negative ions rather than electrons. These so-called ion–ion plasmas allow for the extraction of either positive or negative ion species from the plasma. Early work in Ar/$SF_6$ plasmas show that for 50:50 mixtures (by pressure), both positive and negative ions can be delivered to the surface in equal amounts and with energies that are commensurate with the extraction bias.[34] For the present work, a positive DC bias (20 V) was used to preferentially extract negative species from the plasma. This biasing was found to be

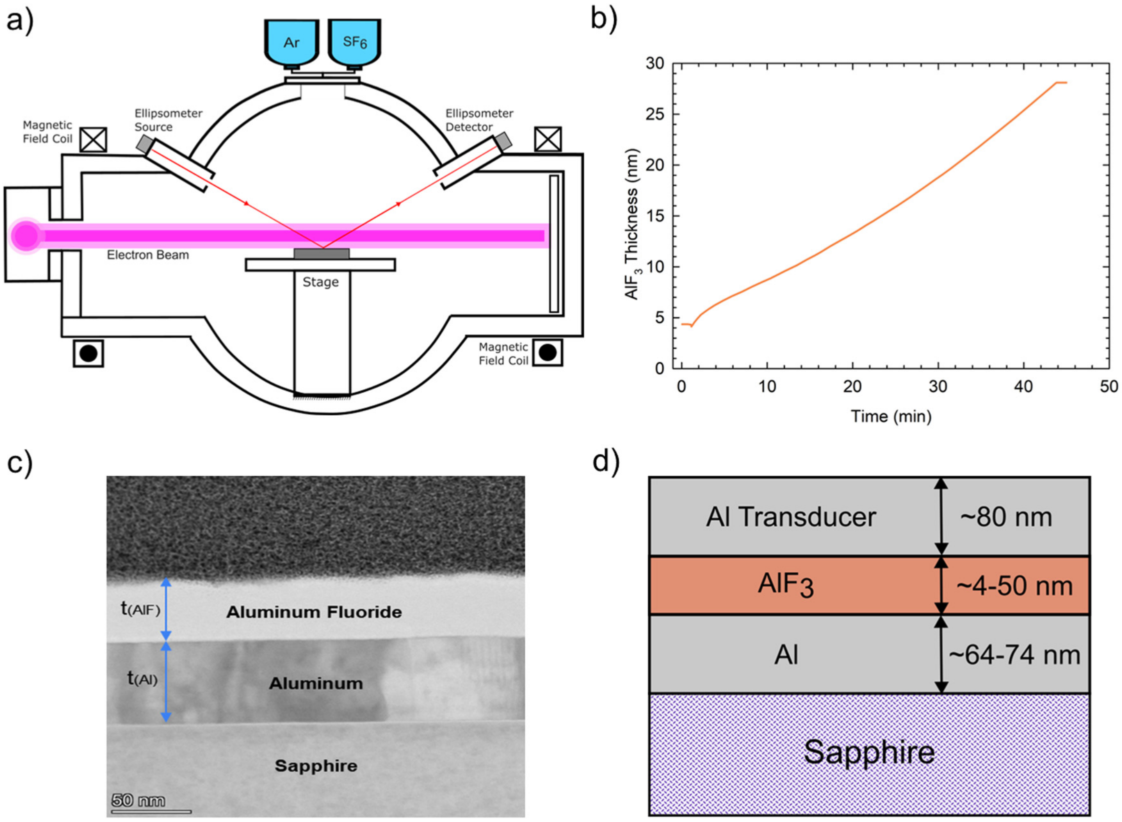

**FIG. 1.** Experimental overview. (a) Schematic of the LAPPS configuration. (b) *In situ* ellipsometry plot monitoring the growth of aluminum fluoride. (c) Cross-sectional TEM image of a sample. (d) Schematic illustration of the layered structure, showing the sapphire substrate, underlying aluminum, grown aluminum fluoride layer of varying thicknesses, and the top 80 nm aluminum transducer layer used for thermoreflectance measurements.

critical to the effective growth of fluoride layers exceeding 10 nm.[1] Under these conditions, the measured surface current is ≈0.05 mA/cm$^2$, which is unlikely to result in any significant increase in surface temperature. While the surface temperature has not been measured, neither the platen nor material is noticeably elevated in temperature even after long treatment times.

The growth process is analogous to aluminum anodization, where thick aluminum oxide films are grown from aluminum substrates. Aluminum anodization is well-established using electrochemical processes[35,36] and has also been demonstrated using plasmas.[37] Regardless of the approach, the process relies on the diffusion of oxygen anions into the material, where they combine with aluminum ions to form aluminum oxide (e.g., $2Al^{3+} + 3O^{2-} \rightarrow Al_2O_3 + 6e^-$). The diffusion of ions is driven by the electric field established across the oxide layer by applying a positive bias to the substrate. For the plasma anodization process utilized in this work, fluorine anions replace oxygen anions as the reactant to enable the production of aluminum fluoride films (e.g., $Al^{3+} + 3F^- \rightarrow AlF_3$). The process is complicated by the presence of a native oxide layer on the as-received aluminum. However, this oxide layer can be removed during processing via direct conversion to a fluoride (e.g., $Al_2O_3 + 6F \rightarrow 2AlF_3 + 3O$) or through an intermediary oxy-fluoride state (e.g., $Al_2O_3 + nF \rightarrow nAlF_xO_y$). A more detailed description of the critical plasma properties and the growth process can be found in earlier work.[38]

Plasma treatments with varying plasma treatment times of 0.3, 3.7, 25.5, 42, 70, and 100 min were conducted. Figure 1(b) presents *in situ* ellipsometry data recorded during the treatment to estimate the film thickness. Once the target film thickness was achieved, the process was stopped, and the last data point (in time) was re-fit to determine the approximate film thickness. For the above-mentioned process times, the resulting fluoride thicknesses were determined to be 6, 9, 14, 28, 35, and 58 nm, respectively (see details in the supplementary material). The optical constants used for determining the thickness of the $AlF_3$ layer can be found in previous work.[24,39] For more precise measurements required for property extraction, we performed transmission electron microscopy (TEM) on cross-sectional samples to accurately determine the physical thicknesses of the AlF3 layers [Fig. 1(c)]. These TEM-derived thicknesses were found to be consistent with cross-sectional TEM–EDX line scans (see the supplementary material), which show a direct correlation between the compositional fluoride signal and the layer boundaries identified in TEM imaging. We attribute the deviation between the values determined by ellipsometry and TEM to this compositional gradient, which creates a continuous refractive index transition that standard discrete-layer optical models do not fully capture. Cross-sectional specimens were prepared using a Thermo Fisher Helios system, and a platinum layer was deposited on the $AlF_3$ films to mitigate damage from the gallium ion beam during thinning. TEM analysis was conducted with a Thermo Fisher Scientific Themis instrument, which revealed $AlF_3$ layer thicknesses of 4.1, 5.9, 11.2, 24.5, 30.3, and 48.1 nm. In addition to thickness verification, the cross-sectional TEM images provide insight into the crystalline state and microstructural features of the films (see Fig. S2 in the supplementary material). These images reveal clear polycrystalline grain boundaries in the underlying aluminum, whereas the $AlF_3$ layer appears featureless, showing no grain boundaries or long-range order. A magnified view of the 48.1 nm sample further highlights this contrast, displaying periodic lattice fringes in aluminum while the $AlF_3$ remains amorphous. These observations confirm that the plasma-synthesized films are dense, continuous, and predominantly amorphous, with no visible microdefects such as pores or cracks. Furthermore, our findings are consistent with numerous previous works showing that $AlF_3$ layers produced via similar processes are amorphous and lack long-range symmetry.[40–43]

We used time-domain thermoreflectance (TDTR), a well-established thin-film thermal conductivity measurement technique,[26,44,45] and steady-state thermoreflectance (SSTR), a recently developed pump–probe technique,[27] to measure the thermal properties of thin $AlF_3$ films. In a TDTR measurement, a modulated pump beam (400 nm) heats the sample surface, while a delayed probe beam (800 nm) detects the temperature decay of the surface via thermoreflectance. The delay time is controlled by a mechanical delay stage, and the signals are collected by a photodetector connected to a lock-in amplifier. The measured signals are fitted using a heat transfer model to extract unknown thermal properties, such as the thermal boundary conductance and thermal conductivity. Similar to TDTR, SSTR is also a pump–probe non-contact technique; in SSTR, steady-state thermal gradients are induced by pump heating. SSTR is a direct measure of thermal conductivity, and thus, unlike TDTR, it does not require prior knowledge of heat capacity due to the steady-state nature of the measurements. Additional details of the TDTR and SSTR measurements and assumptions used in the analysis can be found in previous works.[26,44,46,47]

For the thermal measurements, an additional 80 nm Al film was deposited onto the as-grown $AlF_3$ layers, as shown in Fig. 1(d). This additional aluminum layer acts as the optothermal transducer during thermal measurements and ensures symmetry around the $AlF_3$ layer. As above, the Al transducer for all the samples was created in a single deposition to ensure sample-to-sample consistency. The thermal conductivity of the 80 nm Al transducer and the underlying Al film was determined to be 170 $W\,m^{-1}\,K^{-1}$ from four-point probe electrical resistivity measurements and the Wiedemann–Franz law.[48] This value was used as a fixed input parameter in our thermal models to accurately extract the properties of the $AlF_3$ layer.

To investigate the mechanical properties of the samples, we employed picosecond acoustics.[49] Traditionally, mechanical characterization of thin films often employs techniques like nanoindentation; however, this method can present challenges, particularly for ultra-thin films. The reliability and accuracy of nanoindentation tests on thin films are complicated by factors such as substrate effects, size-dependent properties, and testing conditions.[50,51] It is especially difficult to measure the elastic modulus of films with a thickness less than 100–200 nm due to significant substrate influence.[52] Picosecond acoustic measurements overcome these limitations and enable accurate assessment of the mechanical properties of thin films, as applied here to the $AlF_3$ layers. In our approach, picosecond acoustics was used to measure the cross-plane speed of sound in the samples, which was subsequently used to determine their mechanical properties. In this technique, the Al transducer deposited on the sample partially absorbs the pump laser pulse and undergoes rapid thermal expansion, generating an acoustic (elastic) pulse that propagates away from the surface. The acoustic pulse reflects from interfaces within the sample and returns to the surface, where it modifies the local index of refraction. These changes are detected as variations in the thermoreflectance signal, allowing us to measure the transit time of the acoustic pulse and thereby calculate the speed of sound in the material.

## III. RESULTS: THICKNESS AND CHEMICAL COMPOSITION

To investigate the atomic composition of the $AlF_3$ layers, we performed energy-dispersive x-ray spectroscopy (EDX) analysis using scanning electron microscopy (SEM). SEM/EDX provides quantitative elemental composition data for the samples, as shown in Fig. 2(a) for our $AlF_3$ films. The analysis was carried out using a Thermo Fisher Helios system at an incident angle of 60° and an accelerating voltage of 2 kV. The results, averaged over three spots on each sample, revealed that thicker $AlF_3$ layers exhibited lower aluminum content and higher fluorine content compared to thinner layers; however, both the aluminum and fluorine contents nearly stabilized for $AlF_3$ layers thicker than approximately 20 nm, indicating a consistent stoichiometry in these films. Additionally, variations in oxygen content were observed: Both the thinner $AlF_3$ layers and the thickest sample (subjected to longest processing times) showed higher oxygen levels. In thinner layers, this is likely due to residual native oxide that is not fully removed with short processing times. Indeed, recent work has shown that the volume expansion associated with the complete conversion of $Al_2O_3$ to $AlF_3$ using this process would produce films exceeding ≈15 nm in thickness.[38] In the thickest sample, the extended operating time may increase the liberation of adsorbed water or oxygen from the reactor walls or other surfaces, which could lead to the reoxidation of the sample. No *in situ* plasma diagnostics were available to test this hypothesis. Long processing time can also increase surface roughness,[24] which promotes surface oxidation. While the results are not ideal, the sample provides a useful reference for understanding the impact of oxygen on the thermal and mechanical properties of thick $AlF_3$ films.

To further elucidate the atomic composition and interface structure, we performed cross-sectional EDX mapping and line scans using a SuperXG2 EDX detector integrated with TEM imaging (see Fig. S3 in the supplementary material). The line scans

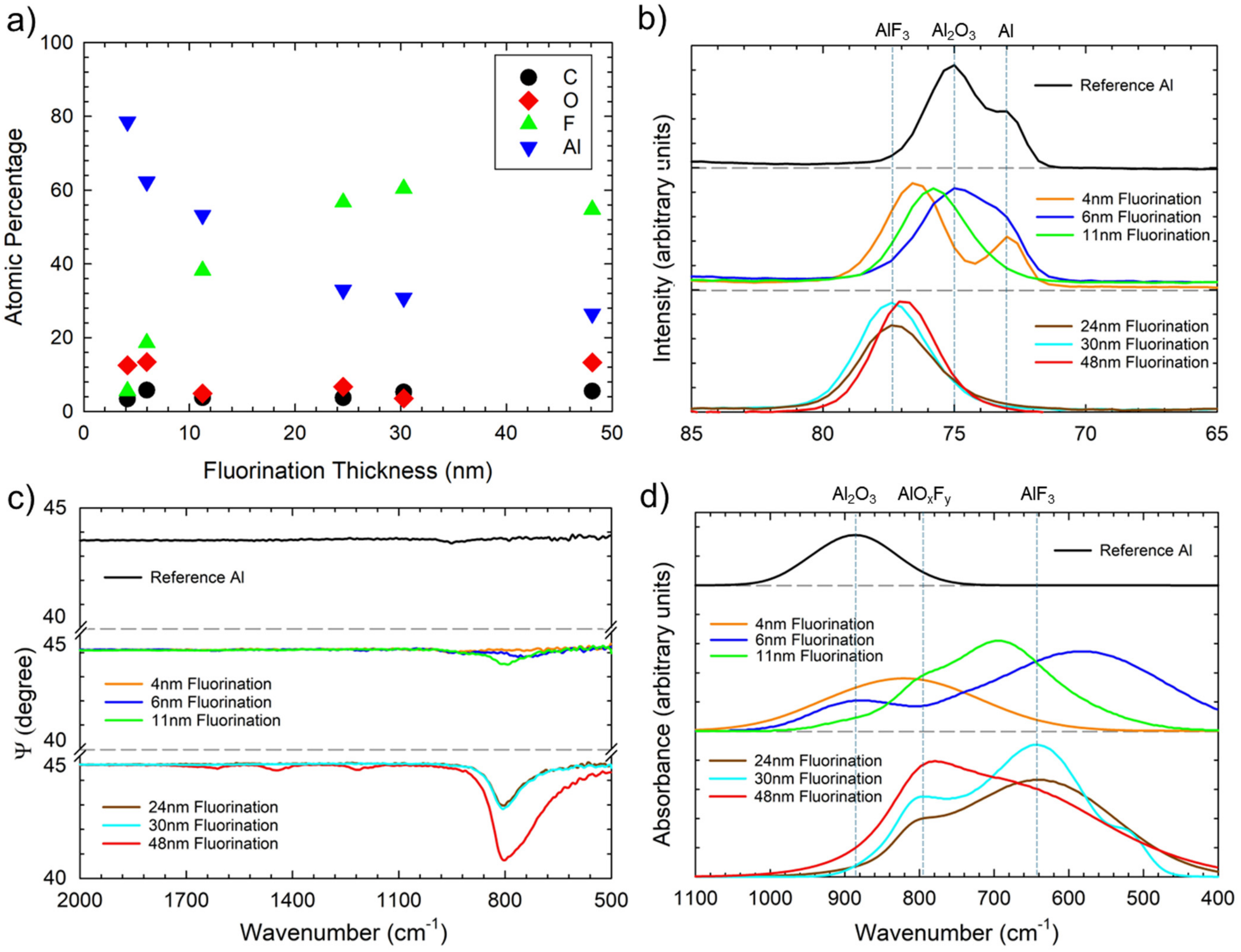

**FIG. 2.** Material characterization of $AlF_3$ layers. (a) EDX analysis showing the atomic percentages of Al, F, C, and O as a function of $AlF_3$ thickness; thicker layers exhibit higher F and lower Al contents. (b) XPS spectra indicating an Al peak at 73 eV, an $Al_2O_3$ peak at 75 eV, and an $AlF_3$ peak at 77–78 eV. (c) Ellipsometric amplitude ratio ($\Psi$) spectra: The intensity of $AlF_3$-related peaks (between 600 and 800 $cm^{-1}$) increases with thickness. (d) Absorbance spectra: Shift from a native oxide peak at 887 $cm^{-1}$ to $AlF_3$-related peaks at 798 and 640 $cm^{-1}$ with increasing fluorination, indicating successful conversion to $AlF_3$.

reveal a compositional gradient at the Al/$AlF_3$ interface, followed by a region of more stable composition in the thicker films. This confirms that while interface effects are present, the bulk of the film reaches a nearly consistent fluorine-rich stoichiometry for thicknesses greater than 20 nm, which correlates with the saturation observed in the material properties. Crucially, when combined with our high-resolution TEM observations (Fig. S2 in the supplementary material), confirming that $AlF_3$ remains predominantly amorphous across all thicknesses, this evidence suggests that the observed property evolution (such as the stiffening of the film) is driven primarily by the change in chemical bonding and stoichiometry (the F/Al ratio) rather than by changes in crystallinity or grain structure. The resulting data also corroborates the compositional trends observed in the SEM/EDX analysis.

To further assess the chemical state of the layers, x-ray photoelectron spectroscopy (XPS) measurements [Fig. 2(b)] were carried out using a PHI Versaprobe III instrument under ultrahigh vacuum conditions (base pressure: $7.2 \times 10^{-8}$ Pa). Data were acquired over a 200 $\mu$m FWHM spot using Al 2p scans with a pass energy of 224 eV (energy resolution of ∼2.2 eV). In the reference sample (untreated aluminum), the XPS spectra display an aluminum peak at approximately 73 eV and a native oxide peak near 75 eV.[53] Even with brief fluorination, these peaks shift or merge in samples thinner than 11 nm, indicating partial conversion from the native oxide. In the 11 nm-thick sample, however, a new peak emerges at about 76 eV, attributed to oxyaluminum fluoride ($AlO_xF_y$) species.[24,54] For samples exceeding 11 nm in thickness (e.g., 24, 30, and 48 nm), a distinct XPS signal appears at around 77.5 eV, suggesting that oxide structures are fully replaced by a stable $AlF_3$ phase as fluorination time increases.[53] In the 48 nm sample, the XPS peak is slightly shifted to lower energies compared to the 24 and 30 nm samples, reflecting its higher oxygen content. In general, signals appearing between about 75 and 77.5 eV may indicate the presence of oxyaluminum fluoride compounds. However, because XPS is inherently surface-sensitive, these measurements primarily capture near-surface chemistry.

To further examine the chemical transformations throughout the film thickness, we performed infrared ellipsometry using an infrared variable-angle spectroscopic ellipsometer (IR-VASE), which can probe the entire fluorinated layer. The ellipsometric data were obtained in the spectral range of 400–2000 $cm^{-1}$ using an IR-VASE Mark II (J.A. Woollam Company), with measurements performed at incident angles of 55° and 65° and a resolution of 8 $cm^{-1}$. The IR-VASE spectra provide insights into the vibrational modes of chemical bonds present, allowing us to monitor changes induced by the fluorination process. The ellipsometry measurements acquire the change in polarization of the light reflected from the sample in terms of amplitude ratio ($\Psi$) [Fig. 2(c)] and phase difference ($\Delta$). These ellipsometric values are related to the complex dielectric function ($\epsilon$) of the sample. Additional details of IR-VASE measurements and analysis can be found in Refs. 55 and 56. We create an isotropic multilayer optical model on this measured ellipsometric data to extract the complex frequency-dependent dielectric function of the $AlF_3$ films. Upon extracting the dielectric function (shown in the supplementary material), the absorbance of the films is calculated using Fresnel equations and depicted in Fig. 2(d).

In the reference sample, a broad absorption peak was observed at 887 $cm^{-1}$, corresponding to the vibrations of Al—O bonds in native aluminum oxide ($Al_2O_3$).[57] Upon fluorination, even with very short exposure times, this peak shifted. For samples with fluorinated layers exceeding 6 nm, the peak at 887 $cm^{-1}$ disappeared entirely, and a new peak stabilized at around 798 $cm^{-1}$. This peak is associated with vibrations related to oxyaluminum fluoride ($AlO_xF_y$) species,[54] indicating the complete transformation of the native oxide into fluoride compounds due to fluorination. Peaks associated with aluminum fluoride ($AlF_3$) appeared at around 640 $cm^{-1}$.[54,58] For samples exceeding 11 nm in thickness, these peaks remained. However, in the sample with a 48 nm thick $AlF_3$ layer, these peaks became broader and their intensity changes. This broadening and change in intensity are likely linked to additional vibrational modes, including the stretching vibrations of Al—O bonds in an octahedral structure,[59] O—H out-of-plane bending modes,[60] and O—C—O bending vibrations,[61] which can arise from changes in surface chemistry caused by higher oxygen content. Additionally, the extended fluorination time required to produce the 48 nm thick layer may have resulted in chamber heating, which allowed other processes (e.g., water desorption) to introduce carbon, oxygen, or hydrogen near the film surface, contributing to these spectral changes. In the 48 nm thick sample, three additional broad peaks at around 1200, 1440, and 1640 $cm^{-1}$ were detected in both $\Psi$ and absorbance plots. These peaks likely correspond to overlapping of C—$F_2$ and C—O asymmetric stretching at 1200 $cm^{-1}$, C—F stretching and C—H bending at 1440 $cm^{-1}$, and C═C stretching at around 1640 $cm^{-1}$,[20,60] These peaks indicate the presence of carbon-containing contaminants, possibly introduced during the prolonged fluorination process.

The XPS and IR-VASE results provide a comprehensive view of the chemical transformation induced by plasma fluorination. These data reveal a gradual transition from native oxide to oxyaluminum fluoride and ultimately to an $AlF_3$ phase. These complementary observations confirm that plasma exposure of more than approximately 40 min (as represented by the 24 nm sample) effectively transforms the native oxide ($Al_2O_3$) into a stable $AlF_3$ layer. This chemical transformation is consistent with the changes observed in the mechanical and thermal characterization, as detailed in Secs. IV and V. This fluorination process not only modifies the surface chemistry but also significantly impacts the material's mechanical and thermal properties.

## IV. RESULTS: THERMAL CONDUCTIVITY

As previously mentioned for the thermal characterization of the $AlF_3$ layers, we employed TDTR and SSTR techniques. In the TDTR measurements, the experimental data, which are proportional to the temperature change on the surface of the sample as a function of pump–probe delay time, were fitted with the solution to the axially symmetric heat equation applied to a multilayer geometry to obtain the effective thermal conductance of the $AlF_3$ layers, where this effective conductance ($G_{Al/AlF3/Al}$) encompasses both the intrinsic thermal conductance of the $AlF_3$ layer and the thermal boundary conductances between the aluminum layers and the $AlF_3$ layer. The effective thermal conductivity ($K_{eff}$) of the $AlF_3$ layers was then calculated by multiplying the effective thermal conductance by the corresponding thicknesses measured from TEM images. Example TDTR data and model fits used to extract $G_{Al/AlF3/Al}$ are shown in the supplementary material.

In the SSTR measurements, the experimental data, which are related to the steady-state temperature changes on the surface of the sample as a function of pump power, was fitted with the solution to the axially symmetric Fourier law (steady state limit of the heat equation) applied to a multilayer geometry, where the combined thermal resistivity of the $AlF_3$ layer and the underlying aluminum are determined from this data analysis.[27] The contribution to this measured thermal resistance of the underlying aluminum is measured separately from the reference sample using the thicknesses obtained from TEM. This aluminum contribution is then subtracted from the total measured resistivity to isolate the thermal resistivity, and thus, the thermal conductivity of the $AlF_3$ layer. Figure 3(a) illustrates a schematic of the TDTR and SSTR techniques, highlighting their different thermal penetration depths.[62] Figure 3(b) shows the effective thermal resistance ($R_{eff}$) of the $AlF_3$ layers obtained using both TDTR and SSTR techniques. For both the methods, a linear relationship is observed between the thermal resistance and the $AlF_3$ thickness for samples thicker than approximately 20 nm. This linearity indicates that, in these thicker samples, the variation in film thickness is the primary contributor to the overall thermal resistance. It is important to note that a

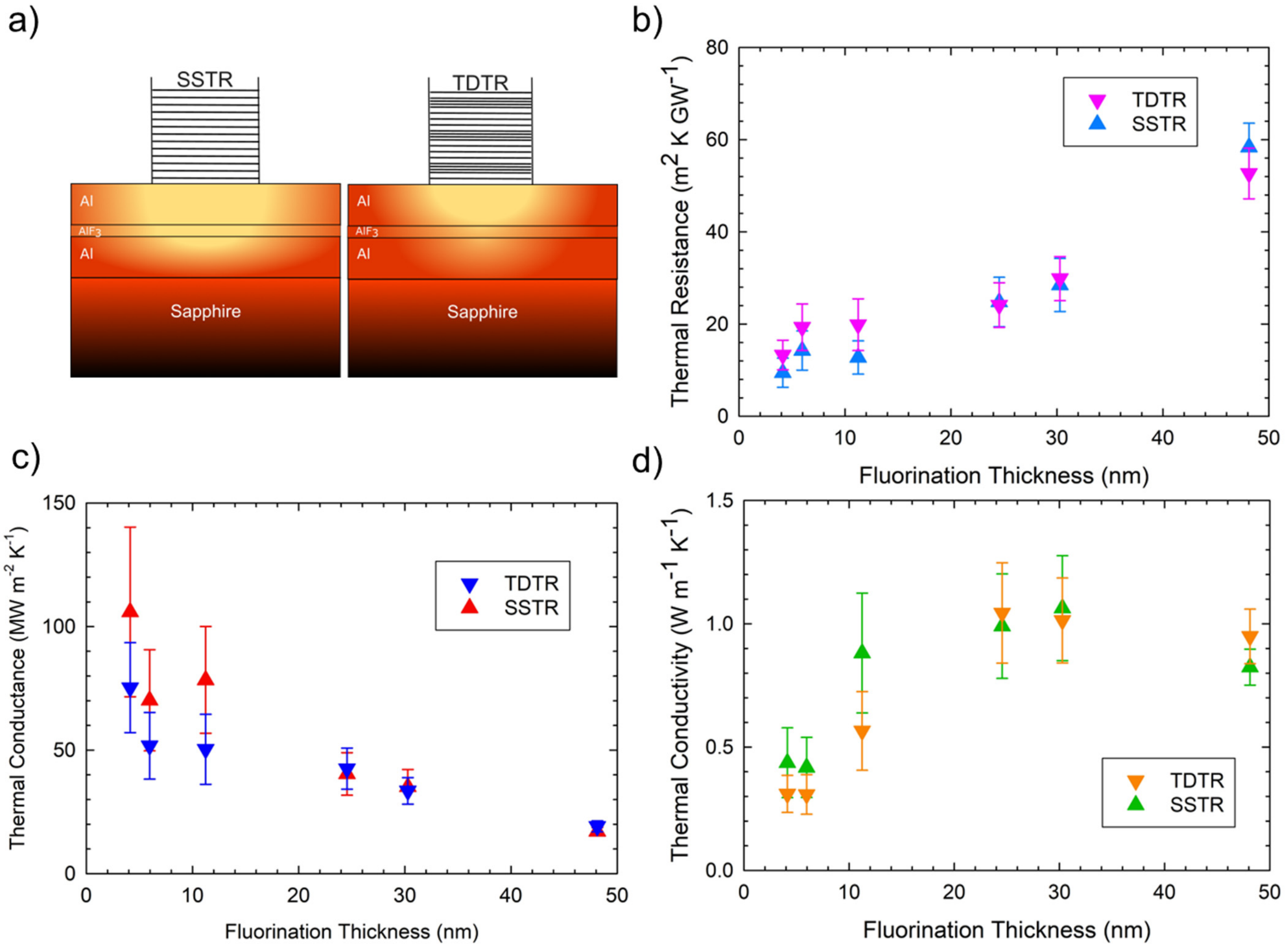

**FIG. 3.** Thermal characterization of $AlF_3$ layers using TDTR and SSTR techniques. (a) Schematic of TDTR and SSTR illustrating different thermal penetration depths. (b) Effective thermal resistance ($R_{\mathrm{eff}}$) vs $AlF_3$ thickness, showing a linear relationship for layers thicker than 20 nm. (c) Effective thermal conductance ($G_{\mathrm{eff}}$) decreases with increasing $AlF_3$ thickness. (d) Effective thermal conductivity ($K_{\mathrm{eff}}$) increases with $AlF_3$ thickness and reaches a plateau for films thicker than 20 nm, indicating saturation of thermal conductivity at higher thicknesses.

nonlinear dependence of thermal resistance on thickness can sometimes indicate the presence of ballistic transport effects and a transition from ballistic to diffusive heat conduction. However, such behavior is not observed in well-studied amorphous materials such as alumina or $SiO_2$, where diffusive transport dominates even at small thicknesses.[63] Our $AlF_3$ layers, which are shown to be amorphous and defect-free in TEM imaging, exhibit a linear resistance–thickness relationship, further supporting the conclusion that the observed changes in thermal resistance arise primarily from variations in chemical composition and film thickness, rather than from any ballistic transport phenomena. The effective thermal conductance for all the samples using both TDTR and SSTR techniques is plotted in Fig. 3(c), demonstrating a decrease in conductance with increasing thickness. Figure 3(d) presents the calculated effective thermal conductivity of the $AlF_3$ layers. The measurements reveal that the thermal conductivity increases with increasing thickness, ranging from approximately 0.3 W $m^{-1}$ $K^{-1}$ for the thinner layers (4 and 6 nm samples) to ∼1.0 W $m^{-1}$ $K^{-1}$ for layers thicker than 20 nm. A direct comparison to prior experimental work is challenging, as there are no previous values reported for the bulk thermal conductivity of $AlF_3$. However, our measured plateau value of ∼1.0 W $m^{-1}$ $K^{-1}$ aligns remarkably well with the theoretical minimum limit of thermal conductivity for amorphous solids,[63] which is predicted to be on the order of 1 W $m^{-1}$ $K^{-1}$ for $AlF_3$.This value is also comparable to that of thin-film amorphous $Al_2O_3$ (∼1.0–1.4 W $m^{-1}$ $K^{-1}$),[64] indicating our process creates a protective layer with similar thermal insulating properties to the native oxide it replaces, while being two orders of magnitude lower than the aluminum film itself ($170\,\mathrm{W\,m^{-1}\,K^{-1}}$). The increasing trend of thermal conductivity with thickness indicates that the thermal transport properties of the $AlF_3$ layers correlate with the changes in chemical composition and material structure resulting from increased fluorination time, as discussed in the previous section.

TDTR and SSTR are uniquely suited for this study since both are single-sided measurements of thermal properties.[26,27] For both techniques, the thermal property measurements exhibit consistent trends with increasing thickness, but differences especially in thinner samples arise due to the varying thermal penetration depths of TDTR and SSTR. The thermal penetration depth in our TDTR measurements is at most $d_p = \sqrt{k/\pi Cf}$, and could be smaller due to thermal boundary resistance effects.[62,65] At our modulation frequency of 8.4 MHz, the thermal wave penetrates approximately 650 nm into the sapphire substrate. In contrast, for SSTR, the probing depth is governed by the pump spot radius ($\approx 1.7\,\mu$m), implying a sensing volume much larger.[27] For the thinnest samples (<20 nm), the thermal resistance of the film is small relative to the spreading resistance of the bulk substrate. Consequently, the measurement signal in SSTR is dominated by the sapphire, making it less sensitive to the specific properties of the ultra-thin layers compared to TDTR. As the film thickness increases beyond 20 nm, the contribution of the film becomes more significant, and the results from both techniques converge.

## V. RESULTS: MECHANICAL CHARACTERIZATION

We use picosecond acoustics to assess the mechanical properties of the $AlF_3$ layers. In our experiments, a strain wave is generated by the rapid thermal expansion of the aluminum transducer layer upon absorption of the pump laser pulse. As shown in Fig. 4(a), this strain wave propagates through the $AlF_3$ and aluminum layers at their respective sound speeds. When the strain wave encounters an interface with a change in acoustic impedance, a portion of the wave is reflected. By measuring the amplitude fluctuations in reflectivity, we can determine the time it takes for the strain wave to travel through each layer. This propagation time, combined with the known film thicknesses, allows us to calculate the longitudinal sound speed for the $AlF_3$ layer.

The picosecond acoustic signals in Fig. 4(b) (reflectivity vs time) were recorded up to 100 ps after the initial heating event. In the reference sample, consisting of an 80 nm aluminum layer (used as a transducer in the $AlF_3$ samples) on sapphire, the second reflectivity peak corresponds to the strain wave reflecting from the Al/sapphire interface. Meanwhile, the trough near the third peak in other samples is simply a second echo from that same interface, so the time intervals between peaks in the reference sample remain unchanged.

In the $AlF_3$ samples, the second peak arises from the strain wave reflecting at the Al/$AlF_3$ interface. Because aluminum and $AlF_3$ have more similar acoustic impedances than aluminum and sapphire, the reflected signal is weaker than in the reference sample. Furthermore, the diffusion of fluorine into the underlying aluminum creates a less distinct boundary, which does not have a sharp enough acoustic impedance mismatch to generate a separate, detectable reflection in our picosecond acoustics measurement. A compositionally graded interface is also observed in our cross-sectional EDX line scans, which support this interpretation (see the supplementary material). Consequently, the third peak corresponds to the Al/sapphire interface, where the larger mismatch in acoustic impedance produces a stronger reflection. This peak in the $AlF_3$ samples shifts in time, depending on the $AlF_3$ layer thickness.

Thus, we derive the sound speed within the $AlF_3$ layer from the total transit time of the acoustic pulse between the first and third peaks ($V_{1-3} = \mathrm{Thickness}_{1-3}/\mathrm{Time}_{1-3}$), corresponding to reflections from the sample surface and the substrate interface, respectively. Knowing the exact thicknesses of each layer and the total transit time between these two peaks ($\mathrm{Time}_{1-3}$), we can quantify the sound speed in the $AlF_3$ layer as $V_{\mathrm{AlF}} = (\mathrm{Thickness}_{1-3}\,V_{1-3} - \mathrm{Thickness}_{Al}\,V_{Al})/\mathrm{Thickness}_{\mathrm{AlF}}$.

Figure 4(c) presents the measured longitudinal sound speed in the $AlF_3$ layers for all the samples. Similar to the thermal properties, the sound speed in the $AlF_3$ layers increases with layer thickness and stabilizes for films thicker than 20 nm. This behavior suggests that the mechanical stiffness of the $AlF_3$ layers is also closely linked to the changes in their chemical composition and structure.

Assuming the $AlF_3$ layer is isotropic, the calculated sound speed can be related to the elastic modulus using $E = \rho v_L^2(1+\nu)(1-2\nu)/(1-\nu)$,[66,67] where $E$ is the elastic modulus and $v_l$ is the measured longitudinal sound speed in the $AlF_3$ layer. The density, $\rho$, was taken as $2.882\,\mathrm{g/cm^3}$, which corresponds to the standard bulk density and is consistent with the previous studies of plasma-synthesized fluoride passivation layers.[25] Poisson's ratio, ν, was assumed to be 0.22 based on experimental work on chemically similar fluoride glass systems, given the scarcity of intrinsic data for amorphous $AlF_3$ thin films.[68]

Using these values, we calculated the elastic modulus, which is presented in Fig. 4(d). We acknowledge that the calculated elastic modulus is sensitive to uncertainties in both the measured and assumed parameters. Therefore, the error bars in Fig. 4(d) represent the propagated uncertainty from all sources, including experimental error in film thickness obtained via cross-sectional TEM and acoustic transit time, as well as the potential variance in assumed material properties. Our sensitivity analysis confirms the impact of these assumptions; for example, calculations show that a 5% variation in density can alter the calculated modulus by up to 7.5%, while a 10% variation in Poisson's ratio can alter it by up to 6.1%. The results show that the elastic modulus increases with $AlF_3$ thickness, reaching values up to approximately 120 GPa for samples with higher fluorine content. This is significantly higher than the modulus of pure aluminum, which is at around 75 GPa.[69] Thinner layers exhibit moduli similar to pure aluminum due to their higher aluminum content. The finding that the $AlF_3$ layer has a higher elastic modulus than aluminum is particularly noteworthy. This increased stiffness is advantageous because the primary purpose of the $AlF_3$ coating is to protect the underlying aluminum in various applications. A stiffer coating layer enhances the mechanical durability and resistance to deformation, which can improve the overall performance and longevity of the coated material.

Our observations align with previous reports that increasing $AlF_3$ content can enhance the elastic modulus in $ZnO—TeO_2$ glasses[68] supporting the beneficial effect of fluorination on mechanical properties. The correlation between higher fluorine

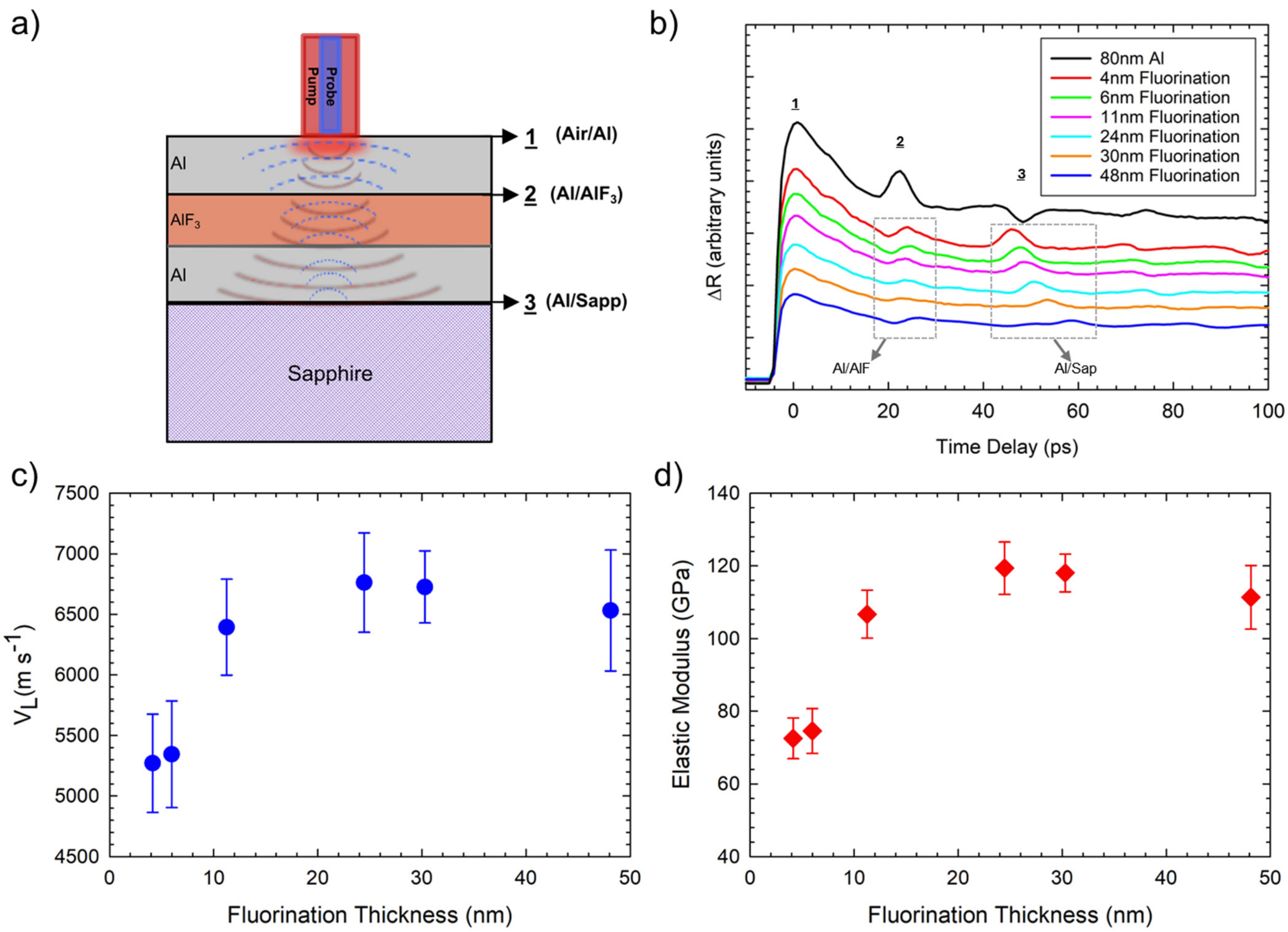

**FIG. 4.** Mechanical characterization of $AlF_3$ layers using picosecond acoustics. (a) Schematic illustration of the picosecond acoustics measurement setup. (b) Reflectivity data as a function of time delay; peaks correspond to reflections from different interfaces, and the absence of a detectable reflection from the $AlF_3$/Al interface due to similar acoustic impedances and the lack of a sharp interface. (c) The measured longitudinal sound speed in $AlF_3$ layers is plotted against layer thickness, revealing an increase in sound speed with increasing thickness and stabilization for films thicker than 20 nm. (d) The calculated elastic modulus of $AlF_3$ layers is shown as a function of thickness, demonstrating an increase in modulus with thickness, which correlates with higher fluorine content and enhanced mechanical stiffness.

content and increased elastic modulus underscores the importance of optimizing the fluorination process to achieve the desired mechanical characteristics in protective coatings.

## VI. CONCLUSION

In this study, we investigated the thermal and mechanical properties of plasma-generated thin aluminum fluoride ($AlF_3$) layers of varying thicknesses grown from aluminum films. The process utilizes an electron beam generated plasma produced in mixtures of Ar and $SF_6$ to simultaneously remove the native oxide and grow an $AlF_3$ passivation layer. Our comprehensive characterization included energy-dispersive x-ray spectroscopy (EDX) for atomic composition, x-ray photoelectron spectroscopy (XPS) and IR-VASE spectroscopy for chemical composition, time-domain thermoreflectance (TDTR) and steady-state thermoreflectance (SSTR) for thermal conductivity, and picosecond acoustics for modulus.

The results demonstrated that both the thermal conductivity and elastic modulus of the $AlF_3$ layers increase with thickness, stabilizing for films thicker than approximately 20 nm. EDX analysis revealed that thicker layers have a higher fluorine-to-aluminum ratio, indicating a transition toward a more stoichiometric $AlF_3$ composition. XPS and IR-VASE spectroscopy confirmed the chemical transformation from a thin native aluminum oxide layer to thicker aluminum fluoride layers with increasing treatment time; shorter fluorination times do not fully remove oxygen, resulting in thin oxyfluoride layers.

The enhanced thermal conductivity in thicker $AlF_3$ layers facilitates better heat dissipation, which is crucial for thermal management in high-power optical devices and advanced lithium-ion batteries as it allows a stable coating to help mitigate thermal runaway by spreading heat from potential hot spots. The measured elastic modulus of ∼120 GPa provides the high mechanical stiffness required to prevent electrode degradation in batteries by reducing the risk of cracking or delamination. Notably, the $AlF_3$ layers exhibited a higher elastic modulus than pure aluminum, highlighting their effectiveness as protective coatings. These findings underscore the importance of optimizing the thickness and composition of $AlF_3$ coatings to achieve the desired thermal and mechanical properties. By tailoring these properties, $AlF_3$ thin films can significantly enhance the performance and durability of devices in ultraviolet optical systems and energy storage applications. We acknowledge certain limitations in the current study. First, ultra-thin films (<4 nm) were not characterized, as these layers approach the resolution limits of our metrology and typically consist of residual native oxide or transitional oxy-fluorides rather than stable $AlF_3$. Additionally, spatial uniformity across the full substrate and long-term environmental stability, such as moisture absorption and corrosion resistance, were not evaluated in this work. Future research will focus on addressing these aspects to further validate process scaling and durability.

Finally, regarding process efficiency, we note that the processing times used in this study (up to 100 min) were selected to maintain a slow, controlled growth regime for fundamental characterization. However, faster processing rates have been demonstrated in previous work. Specifically, replacing the $SF_6$ plasma chemistry with $NF_3$ was shown to provide a 2× increase in the $AlF_3$ growth rate.[25] More generally, the growth rate scales with negative ion density[38] and the latter can be increased with higher electron beam currents.[32] This confirms that the processing time can be effectively reduced by optimizing the operating conditions.

## SUPPLEMENTARY MATERIAL

See the supplementary material for additional figures, tables, and experimental details supporting the results presented in the article. This includes *in situ* ellipsometry growth curves, TEM images of cross-sectional thickness measurements, TEM–EDX compositional mapping, TDTR model fitting example, and extracted dielectric functions.

## ACKNOWLEDGMENTS

This work is partially supported by the NRL base program (D.R.B. and S.G.W.), the Army Research Office, Grant No. W911NF-23-2-0145 (M.M.), the Air Force Office of Scientific Research, Grant No. FA9550-22-1-0456 (P.E.H.), and the Air Force Office of Scientific Research under SBIR Contract No. FA9550-25-C-B005 (A.H.J.).

## AUTHOR DECLARATIONS

### Conflict of Interest

The authors have no conflicts to disclose.

### Author Contributions

**Mohsen Motezaker:** Conceptualization (equal); Data curation (equal); Formal analysis (equal); Methodology (equal); Validation (equal); Writing – original draft (equal). **Andrew H. Jones:** Data curation (supporting); Formal analysis (supporting); Validation (supporting). **David R. Boris:** Project administration (equal); Resources (equal); Supervision (equal); Writing – review & editing (equal). **Scott G. Walton:** Conceptualization (equal); Funding acquisition (equal); Resources (equal); Supervision (equal); Writing – review & editing (equal). **Patrick E. Hopkins:** Conceptualization (equal); Funding acquisition (equal); Methodology (equal); Project administration (equal); Supervision (equal); Writing – review & editing (equal).

## DATA AVAILABILITY

The data that support the findings of this study are available from the corresponding author upon reasonable request.

## REFERENCES

[1] L. V. Rodriguez-de-Marcos, V. D. Wheeler, M. G. Sales, J. G. D. Hoyo, M. Batkis, A. C. Lang, M. A. Quijada, E. J. Wollack, S. G. Walton, and D. R. Boris, "Advances in plasma-based atomic layer processing of $AlF_3$ for the passivation of broadband aluminum mirrors," SPIE Proc. **13100**, 660–672 (2024).

[2] P. López-Reyes, C. Honrado-Benítez, N. Gutiérrez-Luna, Á Ríos-Fernández, L. V. Rodríguez-de Marcos, and J. I. Larruquert, "Far-UV reflectance and stress of narrowband $AlF_3/LaF_3$ multilayers," Opt. Mater. Express **12**(2), 489–502 (2022).

[3] R. Thielsch, "Optical coatings for the DUV/VUV," in *Optical Interference Coatings*, edited by N. Kaiser and H. K. Pulker (Springer, Berlin, 2003), pp. 257–279.

[4] P. K. Tien, "Light waves in thin films and integrated optics," Appl. Opt. **10**(11), 2395–2413 (1971).

[5] J. Hennessy, A. D. Jewell, M. E. Hoenk, and S. Nikzad, "Advances in detector-integrated filter coatings for the far ultraviolet," SPIE Proc. **11821**, 401–406 (2021).

[6] J. A. Tomko, D. R. Boris, S. G. Rosenberg, S. G. Walton, and P. E. Hopkins, "Thermal conductance of aluminum Oxy-fluoride passivation layers," Appl. Phys. Lett. **115**(19), 191901 (2019).

[7] P. Yang, H. Liu, S. Wang, L. Meng, Y. Bai, and J. He, "Functional energetic materials: Simple preparation of fluorinated materials to improve safety, preservation and energy release performance of energetic materials," Colloids Surf., A **694**, 134144 (2024).

[8] X. Wang, H. Tian, S. Ren, P. Zhou, H. Wang, X. Li, and B. Chen, "Effects of a simulated high-energy space environment on a $LaF_3/MgF_2$ multilayer," Opt. Mater. Express **13**(5), 1241–1248 (2023).

[9] A. Koul, A. Ojha, P. Vimal, Y. Pal, S. N. Mahottamananda, S. Subha, and D. Trache, "Enhancement of the energetic performance of solid fuels with metal-fluoropolymer additives," FirePhysChem **4**(2), 131–138 (2024).

[10] S. Wilbrandt, O. Stenzel, H. Nakamura, D. Wulff-Molder, A. Duparré, and N. Kaiser, "Protected and enhanced aluminum mirrors for the VUV," Appl. Opt. **53**(4), A125–A130 (2014).

[11] P. P. K. Agarwal and T. Matsoukas, "Enhanced energetic performance of aluminum nanoparticles by plasma deposition of perfluorinated nanofilms," ACS Appl. Mater. Interfaces **14**(30), 35255–35264 (2022).

[12] M. Ziegler, J. W. Tomm, D. Reeber, T. Elsaesser, U. Zeimer, H. E. Larsen, P. M. Petersen, and P. E. Andersen, "Catastrophic optical mirror damage in diode lasers monitored during single-pulse operation," Appl. Phys. Lett. **94**(19), 191101 (2009).

[13] C. S. Lee, N. Koumvakalis, and M. Bass, "A theoretical model for multiple-pulse laser-induced damage to metal mirrors," J. Appl. Phys. **54**(10), 5727–5731 (1983).

[14] P. B. Corkum, F. Brunel, N. K. Sherman, and T. Srinivasan-Rao, "Thermal response of metals to ultrashort-pulse laser excitation," Phys. Rev. Lett. **61**(25), 2886–2889 (1988).

[15] E. T. Swartz and R. O. Pohl, "Thermal boundary resistance," Rev. Mod. Phys. **61**(3), 605–668 (1989).

[16] C. Monachon, L. Weber, and C. Dames, "Thermal boundary conductance: A materials science perspective," Annu. Rev. Mater. Res. **46**, 433–463 (2016).

[17] J. A. Tomko, A. Giri, B. F. Donovan, D. M. Bubb, S. M. O'Malley, and P. E. Hopkins, "Energy confinement and thermal boundary conductance effects on short-pulsed thermal ablation thresholds in thin films," Phys. Rev. B **96**(1), 014108 (2017).

[18] J.-P. Tourrenc, S. Bouchoule, A. Khadour, J.-C. Harmand, A. Miard, J. Decobert, N. Lagay, X. Lafosse, I. Sagnes, L. Leroy, and J.-L. Oudar, "Thermal optimization of 1.55 $\mu$m OP-VECSEL with hybrid metal–metamorphic mirror for single-mode high power operation," Opt. Quantum Electron. **40**(2–4), 155–165 (2008).

[19] M. J. Zhou, S. F. Wong, C. W. Ong, and Q. Li, "Microstructure and mechanical properties of B4C films deposited by ion beam sputtering," Thin Solid Films **516**(2–4), 336–339 (2007).

[20] B.-H. Liao, C.-C. Lee, C.-C. Jaing, and M.-C. Liu, "Optical and mechanical properties of $AlF_3$ films produced by pulse magnetron sputtering of Al targets with $CF_4/O_2$ gas," Opt. Rev. **16**(4), 505–510 (2009).

[21] M. Mäntymäki, M. Ritala, and M. Leskelä, "Metal fluorides as lithium-ion battery materials: An atomic layer deposition perspective," Coatings **8**(8), 277 (2018).

[22] F. Ding, W. Xu, D. Choi, W. Wang, X. Li, M. H. Engelhard, X. Chen, Z. Yang, and J.-G. Zhang, "Enhanced performance of graphite anode materials by $AlF_3$ coating for lithium-ion batteries," J. Mater. Chem. **22**(25), 12745–12751 (2012).

[23] C. M. Julien and A. Mauger, "Functional behavior of $AlF_3$ coatings for high-performance cathode materials for lithium-ion batteries," AIMS Mater. Sci. **6**(3), 406–440 (2019).

[24] L. V. Rodriguez de Marcos, D. R. Boris, E. Gray, J. G. del Hoyo, A. C. Kozen, J. G. Richardson, S. G. Rosenberg, S. G. Walton, V. Wheeler, E. J. Wollack, J. M. Woodward, and M. A. Quijada, "Room temperature plasma-etching and surface passivation of far-ultraviolet Al mirrors using electron beam generated plasmas," Opt. Mater. Express **11**(3), 740–756 (2021).

[25] L. V. Rodriguez de Marcos, V. D. Wheeler, M. F. Batkis, J. G. del Hoyo, E. N. Jin, S. G. Walton, E. J. Wollack, M. A. Quijada, and D. R. Boris, "Passivation of aluminum mirrors with $SF_6$- or $NF_3$-based plasmas," Opt. Mater. Express **13**(11), 3121–3136 (2023).

[26] D. G. Cahill, "Analysis of heat flow in layered structures for time-domain thermoreflectance," Rev. Sci. Instrum. **75**(12), 5119–5122 (2004).

[27] J. L. Braun, D. H. Olson, J. T. Gaskins, and P. E. Hopkins, "A steady-state thermoreflectance method to measure thermal conductivity," Rev. Sci. Instrum. **90**(2), 024905 (2019).

[28] C. Thomsen, J. Strait, Z. Vardeny, H. J. Maris, J. Tauc, and J. J. Hauser, "Coherent phonon generation and detection by picosecond light pulses," Phys. Rev. Lett. **53**(10), 989–992 (1984).

[29] J. L. Braun, S. W. King, A. Giri, J. T. Gaskins, M. Sato, T. Fujiseki, H. Fujiwara, and P. E. Hopkins, "Breaking network connectivity leads to ultralow thermal conductivities in fully dense amorphous solids," Appl. Phys. Lett. **109**(19), 191905 (2016).

[30] R. A. Neger, R. F. Fensler, M. Lampe, and W. Manheimer, "Large area plasma processing system (LAPPS)," U.S. patent 5,874,807A (1999).

[31] W. M. Manheimer, R. F. Fernsler, M. Lampe, and R. A. Meger, "Theoretical overview of the large-area plasma processing system (LAPPS)," Plasma Sources Sci. Technol. **9**(3), 370 (2000).

[32] S. G. Walton, D. R. Boris, S. C. Hernández, E. H. Lock, T. B. Petrova, G. M. Petrov, and R. F. Fernsler, "Electron beam generated plasmas for ultra low Te processing," ECS J. Solid State Sci. Technol. **4**(6), N5033 (2015).

[33] G. M. Petrov, D. R. Boris, E. H. Lock, T. B. Petrova, R. F. Fernsler, and S. G. Walton, "The influence of magnetic field on electron beam generated plasmas," J. Phys. D: Appl. Phys. **48**(27), 275202 (2015).

[34] S. G. Walton, D. Leonhardt, R. F. Fernsler, and R. A. Meger, "Extraction of positive and negative ions from electron-beam-generated plasmas," Appl. Phys. Lett. **81**(6), 987–989 (2002).

[35] J. O. Bockris, B. E. Conway, and R. E. White, *Modern Aspects of Electrochemistry* (Springer Science & Business Media, 2012).

[36] G. E. Thompson, "Porous anodic alumina: Fabrication, characterization and applications," Thin Solid Films **297**(1–2), 192–201 (1997).

[37] J. F. O'Hanlon, "Plasma anodization of metals and semiconductors," J. Vac. Sci. Technol. **7**(2), 330–338 (1970).

[38] D. R. Boris, M. J. Johnson, V. D. Wheeler, M. G. Sales, L. V. Rodriguez de Marcos, E. J. Wollack, M. A. Quijada, and S. G. Walton, "Electron beam generated ion-ion plasmas produced in Ar/SF6 and Ar/NF3 mixtures for plasma anodization," J. Vac. Sci. Technol. A **44**(1), 013001 (2026).

[39] L. V. R. Marcos, D. R. Boris, J. D. Hoyo, V. Wheeler, J. M. Woodward, J. G. Richardson, S. G. Walton, E. J. Wollack, and M. A. Quijada, "Advanced $AlF_3$-passivated aluminum mirrors for UV astronomy," SPIE Proc. **11820**, 1182005 (2021).

[40] Y. Lee, J. W. DuMont, A. S. Cavanagh, and S. M. George, "Atomic layer deposition of $AlF_3$ using trimethylaluminum and hydrogen fluoride," J. Phys. Chem. C **119**(25), 14185–14194 (2015).

[41] C.-C. Lee, M.-C. Liu, M. Kaneko, K. Nakahira, and Y. Takano, "Characterization of $AlF_3$ thin films at 193 nm by thermal evaporation," Appl. Opt. **44**(34), 7333–7338 (2005).

[42] W. Heitmann, "Vacuum evaporated films of aluminum fluoride," Thin Solid Films **5**(1), 61–67 (1970).

[43] K. Iwahori, M. Furuta, Y. Taki, T. Yamamura, and A. Tanaka, "Optical properties of fluoride thin films deposited by RF magnetron sputtering," Appl. Opt. **45**(19), 4598–4602 (2006).

[44] A. J. Schmidt, X. Chen, and G. Chen, "Pulse accumulation, radial heat conduction, and anisotropic thermal conductivity in pump-probe transient thermoreflectance," Rev. Sci. Instrum. **79**(11), 114902 (2008).

[45] P. Jiang, X. Qian, and R. Yang, "Tutorial: Time-domain thermoreflectance (TDTR) for thermal property characterization of bulk and thin film materials," J. Appl. Phys. **124**(16), 161103 (2018).

[46] P. E. Hopkins, J. R. Serrano, L. M. Phinney, S. P. Kearney, T. W. Grasser, and C. T. Harris, "Criteria for cross-plane dominated thermal transport in multilayer thin film systems during modulated laser heating," J. Heat Transfer **132**, 081302 (2010).

[47] D. G. Cahill, K. Goodson, and A. Majumdar, "Thermometry and thermal transport in micro/nanoscale solid-state devices and structures," J. Heat Transfer **124**(2), 223–241 (2002).

[48] P. D. Desai, H. M. James, and C. Y. Ho, "Electrical resistivity of aluminum and manganese," J. Phys. Chem. Ref. Data **13**(4), 1131–1172 (1984).

[49] G. A. Antonelli, B. Perrin, B. C. Daly, and D. G. Cahill, "Characterization of mechanical and thermal properties using ultrafast optical metrology," MRS Bull. **31**(8), 607–613 (2006).

[50] X. Li and B. Bhushan, "A review of nanoindentation continuous stiffness measurement technique and its applications," Mater. Charact. **48**(1), 11–36 (2002).

[51] W. C. Oliver and G. M. Pharr, "An improved technique for determining hardness and elastic modulus using load and displacement sensing indentation experiments," J. Mater. Res. **7**(6), 1564–1583 (1992).

[52] T. Chudoba, M. Griepentrog, A. Dück, D. Schneider, and F. Richter, "Young's modulus measurements on ultra-thin coatings," J. Mater. Res. **19**(1), 301–314 (2004).

[53] A. H. Jones, J. T. Gaskins, P. E. Hopkins, S. G. Walton, D. R. Boris, J. P. Murphy, L. V. Rodriguez de Marcos, J. Del Hoyo, and M. A. Quijada, "Characterization of $AlF_3$-passivated aluminum mirrors using non-contact thermal metrology," Rev. Sci. Instrum. **96**(2), 024901 (2025).

[54] K. Roodenko, M. D. Halls, Y. Gogte, O. Seitz, J.-F. Veyan, and Y. J. Chabal, "Nature of hydrophilic aluminum fluoride and oxyaluminum fluoride surfaces resulting from XeF2 treatment of Al and $Al_2O_3$," J. Phys. Chem. C **115**(43), 21351–21357 (2011).

[55]W. T. Riffe, S. Zare, K. D. Ardrey, V. K. Champagne, M. Milich, K. Lee, M. Jassas, S. Makarem, E. J. Opila, D. R. Clarke, P. V. Balachandran, and P. E. Hopkins, "Broadband optical phonon scattering reduces the thermal conductivity of multi-cation oxides," Nat. Commun. **16**(1), 3333 (2025).
[56]M. R. Islam, P. Karna, J. A. Tomko, E. R. Hoglund, D. M. Hirt, M. S. B. Hoque, S. Zare, K. Aryana, T. W. Pfeifer, C. Jezewski, A. Giri, C. D. Landon, S. W. King, and P. E. Hopkins, "Evaluating size effects on the thermal conductivity and electron-phonon scattering rates of copper thin films for experimental validation of Matthiessen's rule," Nat. Commun. **15**(1), 9167 (2024).
[57]Ö. İ. Uçar, A. E. Meşe, O. Birbaşar, M. Dündar, and D. Özdemir, "Determination of aluminum oxide thickness on the annealed surface of 8000 series aluminum foil by Fourier transform infrared spectroscopy," in *Light Metals 2017*, edited by A. P. Ratvik (Springer International Publishing, Cham, 2017), pp. 273–278.
[58]M. F. J. Vos, H. C. M. Knoops, W. M. M. Kessels, and A. J. M. Mackus, "Reaction mechanisms during atomic layer deposition of $AlF_3$ using $Al(CH_3)_3$ and $SF_6$ plasma," J. Phys. Chem. C **125**(7), 3913–3923 (2021).
[59]K. Djebaili, Z. Mekhalif, A. Boumaza, and A. Djelloul, "XPS, FTIR, EDX, and XRD analysis of $Al_2O_3$ scales grown on PM2000 alloy," J. Spectrosc. **2015**(1), 1 (2015).
[60]I. O. Faniyi, O. Fasakin, B. Olofinjana, A. S. Adekunle, T. V. Oluwasusi, M. A. Eleruja, and E. O. B. Ajayi, "The comparative analyses of reduced graphene oxide (RGO) prepared via green, mild and chemical approaches," SN Appl. Sci. **1**(10), 1181 (2019).
[61]P. J. Larkin and A. Jackson, "Interpretation of the infrared spectra of metal-stearate salts," Appl. Spectrosc. Pract. **2**(2), 1 (2024).
[62]J. L. Braun and P. E. Hopkins, "Upper limit to the thermal penetration depth during modulated heating of multilayer thin films with pulsed and continuous wave lasers: A numerical study," J. Appl. Phys. **121**(17), 175107 (2017).
[63]D. G. Cahill, S. K. Watson, and R. O. Pohl, "Lower limit to the thermal conductivity of disordered crystals," Phys. Rev. B **46**(10), 6131–6140 (1992).
[64]S.-M. Lee, D. G. Cahill, and T. H. Allen, "Thermal conductivity of sputtered oxide films," Phys. Rev. B **52**(1), 253–257 (1995).
[65]E. A. Scott, J. L. Braun, K. Hattar, J. D. Sugar, J. T. Gaskins, M. Goorsky, S. W. King, and P. E. Hopkins, "Probing thermal conductivity of subsurface, amorphous layers in irradiated diamond," J. Appl. Phys. **129**(5), 055307 (2021).
[66]G. Mavko, T. Mukerji, and J. Dvorkin, *The Rock Physics Handbook* (Cambridge University Press, 2020).
[67]C. Lane, *The Development of a 2D Ultrasonic Array Inspection for Single Crystal Turbine Blades* (Springer Science & Business Media, 2013).
[68]H. A. A. Sidek, S. Rosmawati, M. K. Halimah, K. A. Matori, and Z. A. Talib, "Effect of $AlF_3$ on the density and elastic properties of zinc tellurite glass systems," Materials **5**(8), 1361–1372 (2012).
[69]J. Christudasjustus, T. Larimian, J. Esquivel, S. Gupta, A. A. Darwish, T. Borkar, and R. K. Gupta, "Aluminum alloys with high elastic modulus," Mater. Lett. **320**, 132292 (2022).